Humidity sensor properties of hydrothermally grown rutile-TiO$_2$ microspheres on interdigital electrodes (IDEs)

Yogesh Hase[1], Vidhika Sharma[1], Vidya Doiphode[1], Ashish Waghmare[1], Ashvini Punde[1], Pratibha Shinde[1], Shruti Shah[1], Swati Rahane[1], Priti Vairale[1], Bharat Bade[1], Yogesh Jadhav[1], Mohit Prasad[1,*], Sachin Rondiya[2], Avinash Rokade[3], and Sandesh Jadkar[3,*]

[1] School of Energy Studies, Savitribai Phule Pune University, Pune 411007, India

[2] Department of Materials, Imperial College London, South Kensington, London SW7 2AZ, UK

[3] Department of Physics, Savitribai Phule Pune University, Pune 411007, India

ABSTRACT

Rutile-TiO$_2$ microspheres were synthesized by the single-step hydrothermal method and were subsequently annealed in an argon environment at 200 °C, 400 °C, and 600 °C. The influence of annealing temperature on structural, optical, morphological, and humidity sensing performance of rutile-TiO$_2$ microspheres was examined. As-synthesized and annealed rutile-TiO$_2$ microspheres were characterized using different characterization techniques. SEM confirmed the spherical shape morphology of TiO2 microspheres. XRD confirmed the tetragonal structure and rutile phase of TiO$_2$ microspheres. The rutile phase of TiO$_2$ was also confirmed by Raman spectroscopy. No significant change in the bandgap has been observed in rutile-TiO$_2$ with increased annealing temperature. The presence of various chemical groups in rutile-TiO$_2$ microspheres was studied using FTIR spectroscopy. The Brunauer–Emmett–Teller (BET) and Barrett–Joyner–Halenda (BJH) analysis showed a decrease in surface area and pore volume and an increase in average pore radius with an increase in annealing temperature. The humidity sensing performance of TiO$_2$ microspheres thin films deposited on interdigital electrodes (IDEs) was studied between 11 to 97% relative humidity (RH). The humidity sensor fabricated using rutile-TiO$_2$ microspheres annealed at 600 °C showed excellent humidity sensing properties. The sensor has the highest sensitivity ($\sim$ 71.5%), fast response, and recovery time of $\sim$ 11.1 s and $\sim$ 0.8 s, respectively.

Address correspondence to E-mail: mohitprasad7@gmail.com; sandesh@physics.unipune.ac.in

Springer

1 Introduction

Humidity detection and measurement are essential for agriculture, industry, health care, meteorology, air conditioning, and environmental monitoring [1–5]. The criteria such as rapid response and recovery time, good repeatability, excellent sensitivity, linearity, and a small hysteresis loop are general requirements for a good humidity sensor. There are several materials used as a sensitive layer for humidity sensors devices. The humidity sensors are classified into two categories, relative humidity sensors and absolute humidity sensors. Most of the sensors are relative humidity sensors, which are further classified into ceramic and polymer humidity sensors [6]. The polymer and ceramic types of humidity sensing materials operate via a proton conduction mechanism [7, 8]. Metal oxide ceramics-based humidity sensors possess high sensitivity high chemical and mechanical stability compared to polymer materials counterparts [9–11]. TiO_2, SiO_2, SnO_2, ZnO, Al_2O_3, WO_3 are the most popular ceramic-type metal oxide materials used for humidity sensing devices [12, 13]. Among these, TiO_2 is the most studied material, which has many applications in diverse fields such as anti-fogging surface coatings, solar cells [14], gas sensors [15], energy harvesting/storage [16], photocatalysis [17], etc. It also exhibits good electrochemical stability, hydrophilicity, and surface roughness. It is an n-type transition metal oxide semiconductor material with three phases: anatase, brookite, and rutile. Anatase and rutile phases are more stable than brookite. Anatase and rutile TiO_2 have tetragonal structures, whereas brookite has an orthorhombic structure. The rutile phase is more stable than anatase at high temperatures and pressure. Nanostructures of TiO_2 can be synthesized by various methods such as physical vapor deposition [18], wet chemical method [19], sol–gel method [20], electrodeposition method [21], chemical vapor deposition [22], solution combustion method [23], and hydrothermal method [24], etc. The morphology of the sensing material also plays a vital role in humidity sensing performance. The performance of different nanostructures such as nanowires [25], nanobelts [26], nanotetrapods [27], and nanorods [28] was studied for humidity sensing. The hydrothermal method is the most popular for the large-scale synthesis of materials among these methods. Different morphologies of TiO_2, like nanobelts [29], nanowires [30], nanoflowers [31], and nanorods [32], have been successfully synthesized by the hydrothermal method. Chow et al. [33] had prepared TiO_2 thin films by reactive sputtering. Nevertheless, the response time of the humidity sensor obtained by this method is relatively long. Zhang et al. [34] also prepared highly ordered TiO_2 nanotubes by anodic oxidation. However, the humidity sensor's response and recovery time were quite large (100 s and 190 s, respectively). Wu et al. [35] fabricated a TiO_2 and TEOS-Nafion composite by hydrothermal method. They reported that the response time at 97% of relative humidity was much longer than the humidity range between 12 and 76%. Most of the reports show that TiO_2 has an excellent response to high humidity level (above 50% RH), and fail to gain response to low humidity level (below 30% RH) [36, 37]. In order to enhance the response to low humidity level we have used interdigital electrode. Zhao et al. [38] found that the interdigital electrode gap size influences the humidity sensor's response to surface electrical conduction mechanisms. After the synthesis process, the annealing treatment improves lattice structure and crystallinity and reduces material defects. In the present study, we have fabricated IDE by a simple copper itching process. The synthesized TiO_2 microspheres were deposited on these IDEs and thereby we have studied the humidity response. The sensitivity, as well as response to humidity, mainly depends on distance between two electrodes. In fabricated IDEs the distance between electrodes enable fast charge transfer rate which results in better sensitivity, fast response and recovery time.

Most research on TiO_2 for humidity sensors focuses on Ti^{3+} defect sites. The presence of Ti^{3+} defects and the oxygen vacancies on the surface of TiO_2 directly affects the performance of the humidity sensor. A large number of oxygen vacancies for TiO_2 material can enhance the ionization of adsorbed water molecules and speed up the conduction process [39]. Huali et al. [40] reported that TiO_2 sample annealed in an atmosphere of lower oxygen content such as Ar, N_2 contains a high density of oxygen vacancies which was also confirmed by XPS and ESR results. With this motivation, the present study attempts to synthesize and characterize TiO_2 microspheres and explore their possible use as a humidity sensor. In the present work, the TiO_2 microspheres are synthesized by hydrothermal method and subsequently annealed in Ar at 200 °C, 400 °C, and

600 °C. The influence of annealing temperature in the Ar atmosphere on surface morphology structural and optical properties are investigated. Finally, humidity sensors are fabricated using as-synthesized and annealed TiO_2 microspheres on interdigital electrodes instead of conventional FTO substrate to study the humidity sensing performance. We found that TiO_2 microspheres and IDEs based humidity sensors had significantly enhanced response and recovery time compared to conventional ones.

2 Experimental

2.1 Synthesis of TiO_2 microspheres

TiO_2 microspheres were synthesized via the hydrothermal method. In a typical procedure, 10 ml of titanium butoxide [$Ti(C_4H_9O)_4$, Sigma Aldrich] was drop-wise added into the mixture of 20 ml hydrochloric acid [HCl, Sigma Aldrich] and 30 ml distilled water in a ratio of 1:2:3. The above solution was stirred at room temperature for an hour using a magnetic stirrer. The solution was then transferred into a 100 ml stainless steel autoclave. The autoclave was sealed tightly and placed in an oven at 150 °C for 24 h. After completing the reaction, the autoclave was allowed to cool naturally, and the white precipitate was separated by centrifugation. Next, the residue was washed several times with distilled water and ethanol. Finally, the washed residue was dried under an IR lamp. The as-synthesized TiO_2 powder was then annealed in a tube furnace at 200 °C, 400 °C, and 600 °C in the Ar atmosphere for 2 h. The schematic of the synthesis of TiO_2 powder is depicted in Fig. 1.
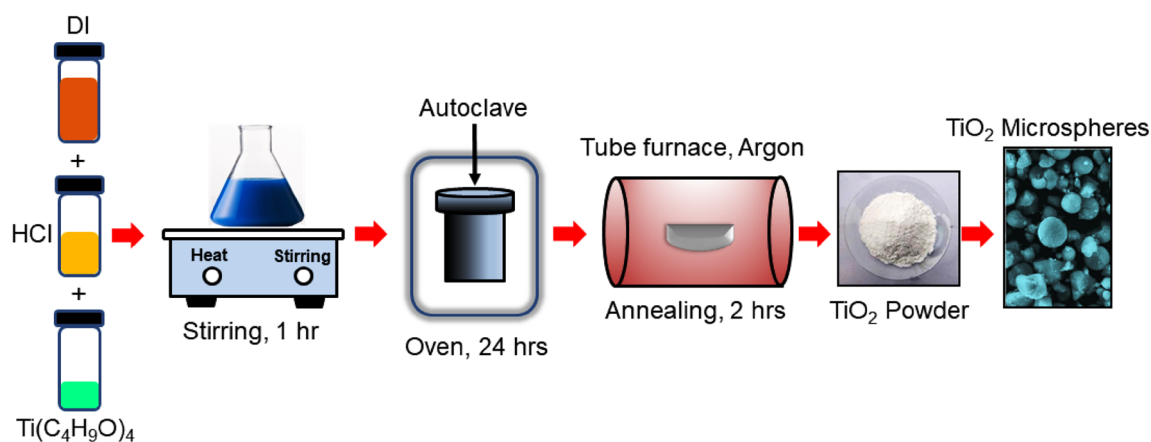
2.2 Material characterization

As-synthesized and annealed TiO_2 powder were characterized using various characterization techniques. The crystallinity and phase formation of TiO_2 was confirmed by an x-ray diffractometer (Bruker D8 Advance, Germany) using CuK_λ ($\lambda = 1.54$ Å) radiation source in the range $2\theta = 20°$–$80°$. Raman spectroscopy instrument (Reinshaw microscope) in the range 100–800 cm^{-1} was used to record the Raman spectra using a source wavelength of 532 nm. The UV–Visible optical absorption spectra were measured using JASCO V-670 (Japan) UV–Visible spectrophotometer. Scanning electron micrographs were recorded using JEOL JSM-6360-LA scanning electron microscopy (SEM). The FTIR spectra of TiO_2 were recorded with JASCO, FTIR-6100 FTIR spectrophotometer in the range of 500–4000 cm^{-1}. The BET (Braunauer–Emmet–Teller) studies were carried out using Quantachrome Instrument to analyze the compounds' pore size and surface area.

2.3 Sensor design, fabrication, and characterization

The interdigital electrode (IDE) finger pattern was initially printed on a toner transfer paper (Glossy Paper) by the HP LaserJet Pro M202dw printer. This IDE pattern was then transferred to a clean Cu clad plate by heat treatment. The copper-clad plate was then dipped in 1 M of ferric chloride ($FeCl_3$) solution for the Cu etching process. After completing the etching process, the Cu IDE finger pattern was obtained. The schematic of the IDE pattern is shown in Fig. 2.
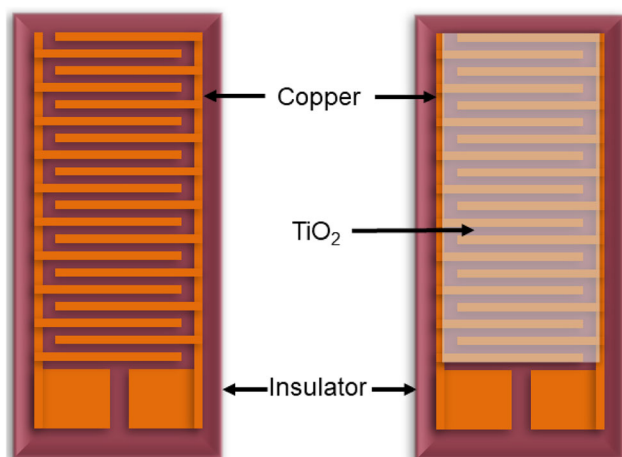

Fig. 1 Schematic of the synthesis process of TiO_2 powder by hydrothermal method

Fig. 2 Schematic of the interdigital electrode (IDE) pattern prepared and used in the present study

The sensing area of the substrate is 1.08 cm^2, with 20 interdigitated fingers. The gap between two consecutive fingers is $\sim$ 500 μm. The TiO$_2$ powder was mixed with ethanol and ground in a mortar to form a paste. The paste was then transferred and coated on IDE substrate by a thin brush. The film was dried naturally in the air overnight before testing. The thickness of all TiO$_2$ films calculated by the gravimetric method was found to be 9.5 μm. Figure 3 shows the schematic of the humidity sensing performance measurement setup used in the present study.

The humidity sensing performance of the TiO$_2$ sensor was tested at different humidity levels. The saturated salts are used to maintain different relative humidity levels, LiCl (11%), CH$_3$CO$_2$K (22%), MgCl$_2$ (33%), K$_2$CO$_3$ (43%), Mg(NO$_3$)$_2$ (52%), KI (68%), NaCl (75%), (NH$_4$)$_2$SO$_4$ (80%), KCl (84%), KNO$_3$ (93%) and K$_2$SO$_4$ (97%). These salts' relative humidity (% RH) was tested on a portable Dewpoint hygrometer HI

9565 (HANNA instruments) with a HI706023 sensing probe. All the electrical measurements were carried out using a source meter (Keithley 2450).

3 Results and discussion

3.1 Morphological studies

The surface morphology of as-synthesized and annealed rutile-TiO$_2$ nanoparticles was studied using scanning electron microscopy (SEM) analysis. Figure 4 shows SEM images of as-synthesized and annealed rutile-TiO$_2$ nanoparticles.

The morphology of rutile-TiO$_2$ is microspheres. The SEM images show that the average microsphere size increases with annealing temperature; however, the surface morphology remains the same. The average diameter of the TiO$_2$ microspheres is $\sim$ 4.46 μm for as-synthesized rutile-TiO$_2$ and $\sim$ 5.23 μm, $\sim$ 6.71 μm and $\sim$ 7.38 μm for rutile-TiO$_2$ annealed at 200 °C, 400 °C, and 600 °C, respectively.

3.2 X-ray diffraction (XRD) analysis

Figure 5 shows the XRD pattern of as-synthesized and annealed TiO$_2$ nanoparticles. The presence of multiple peaks in the diffraction pattern indicates that all films are polycrystalline. As seen, major diffraction peaks are observed at $2\theta \sim 27.22°$, 35.83°, 38.94°, 41.03°, 43.85°, 54.07°, 56.38°, 62.50°, 63.77°, 68.71° and 69.49° which are associated with (110), (101), (200), (111), (210), (211), (220), (002), (310), (301) and (112) planes respectively. These peaks are compared with the standard JCPDS data card #01-078-1510 and imply the tetragonal rutile-TiO$_2$ phase
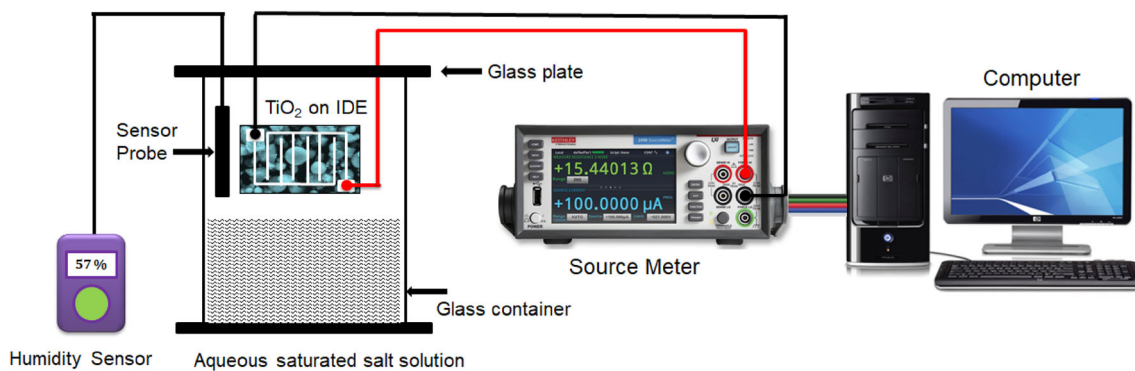

Fig. 3 Schematic of the humidity sensing performance measurement setup used in the present study

Fig. 4 SEM images of as-synthesized and annealed rutile-TiO_2 prepared by the hydrothermal method
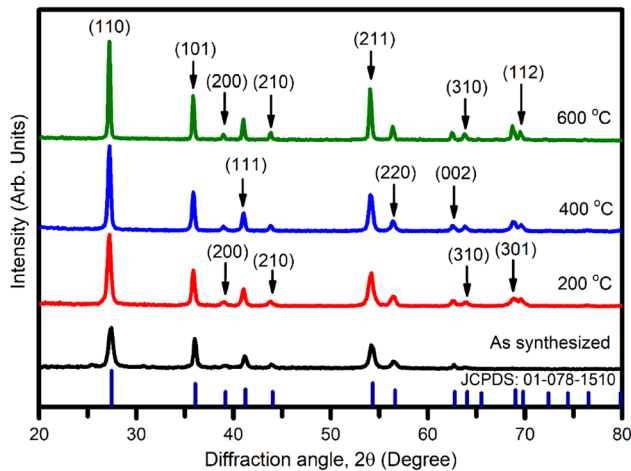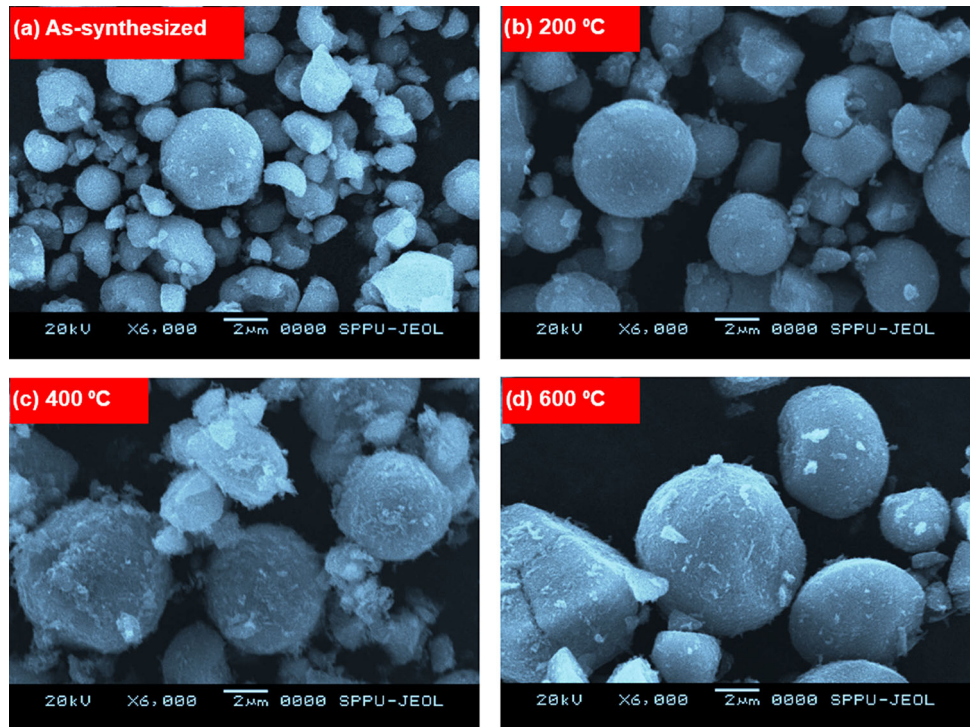

Fig. 5 XRD pattern of as-synthesized and annealed TiO_2 microspheres powder prepared by hydrothermal method

formation. No diffraction peaks of anatase or brookite phase have been detected in the XRD pattern, ensuring the synthesis of high-purity rutile-TiO_2 nanoparticles using the hydrothermal method. The most intense peak corresponds to the (110) plane, and its intensity increases with an increase in annealing temperature, signifying an increase in crystallinity.

The following equation determines the lattice parameters a and c [41],

$$\frac{1}{d_{hkl}^2} = \frac{h^2 + k^2}{a^2} + \frac{l^2}{c^2}. \tag{1}$$

The calculated values of lattice constants are $a = b = 4.60$ Å and $c = 2.96$ Å, which agree with the standard reported values for tetragonal rutile-TiO_2. For the as-deposited rutile-TiO_2 film, the absence of diffraction peaks at $2\theta \sim 68.71°$ and $69.49°$ corresponding to the (301) and (112) planes may be due to insufficient heat energy to complete the crystallization process.

The crystallite size (D) of rutile-TiO_2 was calculated from (110) peak using Debye–Scherrer's equation,

$$D = \frac{k}{\beta \cos \theta}, \tag{2}$$

where k is the particle shape factor and taken as 0.9 for spherical shape nanoparticles, λ is the x-ray source wavelength, β is the full width at half maximum (FWHM), and θ represents Bragg's diffraction angle. As seen, the values of FWHM for rutile-TiO_2 films decreases with an increase in annealing temperature, suggesting an increase in crystallite size with annealing temperature. The values of FWHM and crystallite size of rutile-TiO_2 samples are listed in Table 1. The crystallite size for as-synthesized rutile-

Table 1 Crystallite size, dislocation density, and microstrain of rutile TiO_2 at the various annealing temperatures

Annealing temperature (°C)	FWHM (deg.)	Crystallite size (d_{x-ray}) (nm)	Dislocation density (δ) (m^{-2})	Micro-strain (ε)
As synthesized	0.68	12.02	6.92×10^{15}	12.26×10^{-3}
200	0.43	19.00	2.77×10^{15}	7.75×10^{-3}
400	0.32	25.54	1.53×10^{15}	5.77×10^{-3}
600	0.26	31.43	1.01×10^{15}	4.69×10^{-3}

TiO_2 is found ~ 12 nm and it increases with annealing temperature.

A dislocation is a crystallographic defect or irregularity within a crystal structure that strongly influences the material properties. The dislocation density (δ) is the length of dislocation lines per unit volume of the crystal and was calculated using the relation [42],

$$\delta = \frac{n}{D^2}, \tag{3}$$

where n is the factor that is equal to unity for minimum dislocation density and D is the crystallite size.

The calculated values of dislocation density are listed in Table 1. It is observed that the dislocation density decreases with an increase in annealing temperature, implying a decrease in lattice imperfections in rutile-TiO_2 nanoparticles.

Lattice micro-strain (ε) in a crystal occurs due to the unit cell's displacements from their normal position. It arises in the rutile-TiO_2 due to lattice misfit, such as imperfections like dislocation, stacking fault probability, and lattice distortion. The micro-strain was calculated using the equation,

$$\varepsilon = \frac{\beta}{4 \tan \theta}, \tag{4}$$

where β is the full width at half maximum and θ is the Bragg angle. The micro-strain for as-deposited rutile-TiO_2 is found ~ 12.2, and it decreases with an increase in annealing temperature, implying a decrease in lattice imperfections in rutile-TiO_2. The calculated values of micro-strain are listed in Table 1.

3.3 Raman spectroscopy studies

The Raman spectra of as-synthesized and annealed TiO_2 are shown in Fig. 6. As seen, the Raman spectra consist of four Raman bands at ~ 604 cm^{-1}, ~ 441 cm^{-1}, ~ 225 cm^{-1}, and ~ 136 cm^{-1}, which are characteristic vibrations of rutile-TiO_2. The
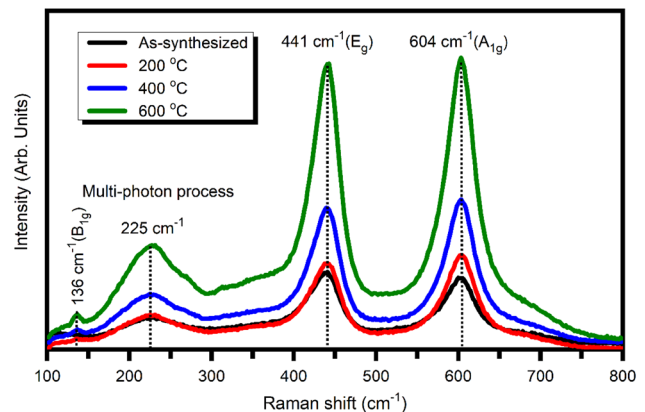
Fig. 6 Raman spectra of as-synthesized and annealed rutile-TiO_2 microspheres powder prepared by hydrothermal method

distinct stretching peaks at ~ 441 cm^{-1} and ~ 604 cm^{-1} correspond to the symmetries of E_g and A_{1g} modes of rutile-TiO_2, respectively.

The band positions of TiO_2 are in good agreement with previous reports for the rutile phase [43]. The intensity of E_g and A_{1g} modes increases, whereas FWHM decreases with an increase in annealing temperature. The FWHM values of the mentioned modes are listed in Table 2.

Another tiny peak at ~ 225 cm^{-1} arises from the multiple phonon scattering processes [44]. Furthermore, no Raman active modes due to other organic impurity phases are observed, indicating the formation of pure rutile-TiO_2 phase by the hydrothermal method. These results are analogous to the XRD analysis.

3.4 Fourier transform infrared (FTIR) spectroscopy analysis

To investigate the presence of various chemical groups in as-synthesized and annealed TiO_2, Fourier transform infrared (FTIR) spectroscopy was used. Figure 7 shows the FTIR spectra of hydrothermally synthesized TiO_2 in 500–4000 cm^{-1}. The strong

Table 2 FWHM values of rutile TiO_2 at the various annealing temperatures

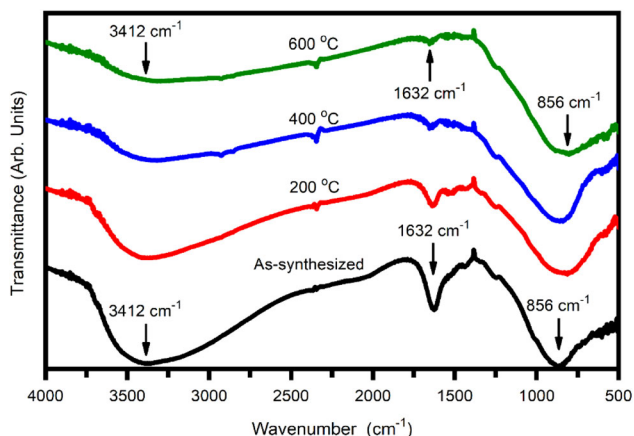| Annealing temperature (°C)	FWHM (cm^{-1})@ 441 cm^{-1}	FWHM (cm^{-1})@ 604 cm^{-1}
As synthesized	41.4	47.1
200	40.3	44.9
400	38.8	43.9
600	36.2	42.6

Fig. 7 FTIR spectrum of hydrothermally synthesized rutile-TiO_2 microspheres powder and annealed at different temperatures

absorption broad-band below 1000 cm^{-1} corresponds to the characteristic Ti–O and Ti–O–Ti stretching and bending vibrational modes for rutile-TiO_2. The vibrational peak $\sim$ 3412 cm^{-1} corresponds to the O–H stretching vibrations, whereas the peak $\sim$ 1632 cm^{-1} corresponds to the hydroxyl group of the water molecule. With an increase in annealing temperature, the absorption intensity in all bands gradually reduced.
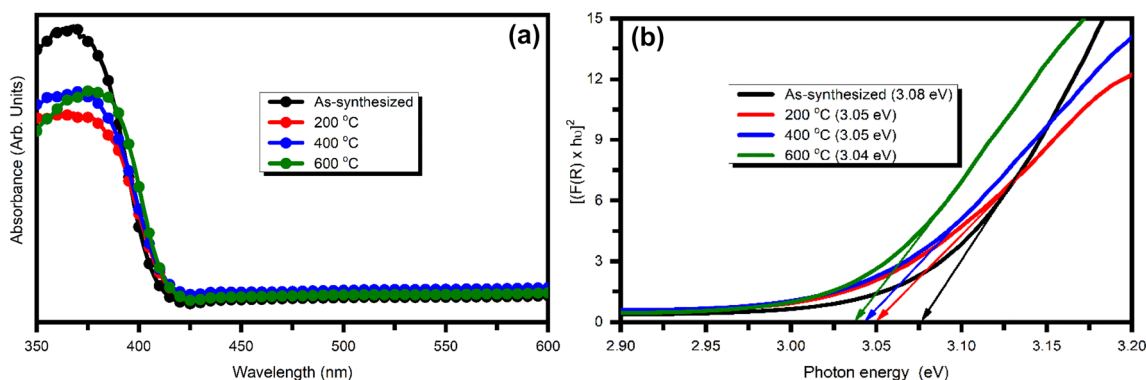
3.5 UV–Visible spectroscopy analysis

The optical properties of rutile-TiO_2 were investigated using UV–Visible spectroscopy. Figure 8a shows the optical absorption spectra of as-synthesized and annealed rutile-TiO_2 nanoparticles in the range of 200–800 nm. It exhibits a sharp absorption edge in 397 nm to 410 nm. A red-shift in absorption edge has been observed with increase in annealing temperature, which may be due to increase in crystallite size with increase in annealing temperature. The XRD analysis support this conjecture.

To calculate the band gap of rutile-TiO_2, the diffuse reflectance (R) value has been converted to equivalent absorption and extinction coefficient value [F(R)] using Kubelka–Munk transformation [45],

$$F(R) = \frac{(1-R)^2}{2R}, \qquad (5)$$

Figure 8b shows a typical Tauc plot used to estimate the direct band gap using Kubelka–Munk transformation for rutile-TiO_2 synthesized at different annealing temperatures by hydrothermal method. No significant change in the band gap has been observed in rutile-TiO_2 with increased annealing temperature. However, it decreases slightly from 3.08 eV for the sample annealed at 600 °C to 3.03 eV

Fig. 8 a Optical absorption spectra of as-synthesized and annealed rutile-TiO_2 microspheres and **b** Typical *Tauc's* plot used to estimate the direct bandgap using Kubelka–Munk transformation

for the as-synthesized rutile-TiO$_2$ sample. These values are shown in Fig. 8b.

3.6 BET analysis

The Brunauer–Emmett–Teller (BET) method is commonly applied to calculate the specific surface area based on nitrogen adsorption isotherm measurements [46–48]. Figure 9a–d represents the BET and *Barrett–Joyner–Halenda* (BJH) analysis of as-synthesized and annealed TiO$_2$ at various temperatures. Figure 9a shows the nitrogen adsorption–desorption isotherms for TiO$_2$. It exhibits a type IV isotherm corresponding to a mesoporous structure with a relative pressure between 0 and 1.

In addition, the presence of the hysteresis loop provides information about the pore size. The values of BET results for surface area, average pore radius, and pore volume of TiO$_2$ at the various annealing temperature are summarized in Table 3.

As seen from Table 3, the surface area of TiO$_2$ decreased with an increase in annealing temperature. It can be attributed to the increase in crystallite size and crystallinity of TiO$_2$ with an increase in

annealing temperature. The XRD analysis further supports this (Fig. 5). As the temperature is elevated to 600 °C, the total pore volume decreases. We think that decrease in pore volume may be due to the collapse of pore structure and aggregation/merging of multiple grains into bulk due to crystal growth. Therefore, the porosity decreases with an increase in annealing temperature. As a result, there is a reduction in the defect density, which improves the electrical conductivity. These results agree with the previously reported work [49, 50]. Therefore, the obtained BET and BHJ results are desirable for the enhanced sensing performance of TiO$_2$ based humidity sensors.

3.7 Humidity sensor performance

The humidity sensing behavior of the TiO$_2$ microsphere was investigated by fabricating the two probe IDE devices and then introducing them into different relative humidity (RH) conditions, which were attained using saturated salt solutions at room temperature. Figure 10 shows the current–voltage (I–V) characteristics of the TiO$_2$ microsphere (annealed at
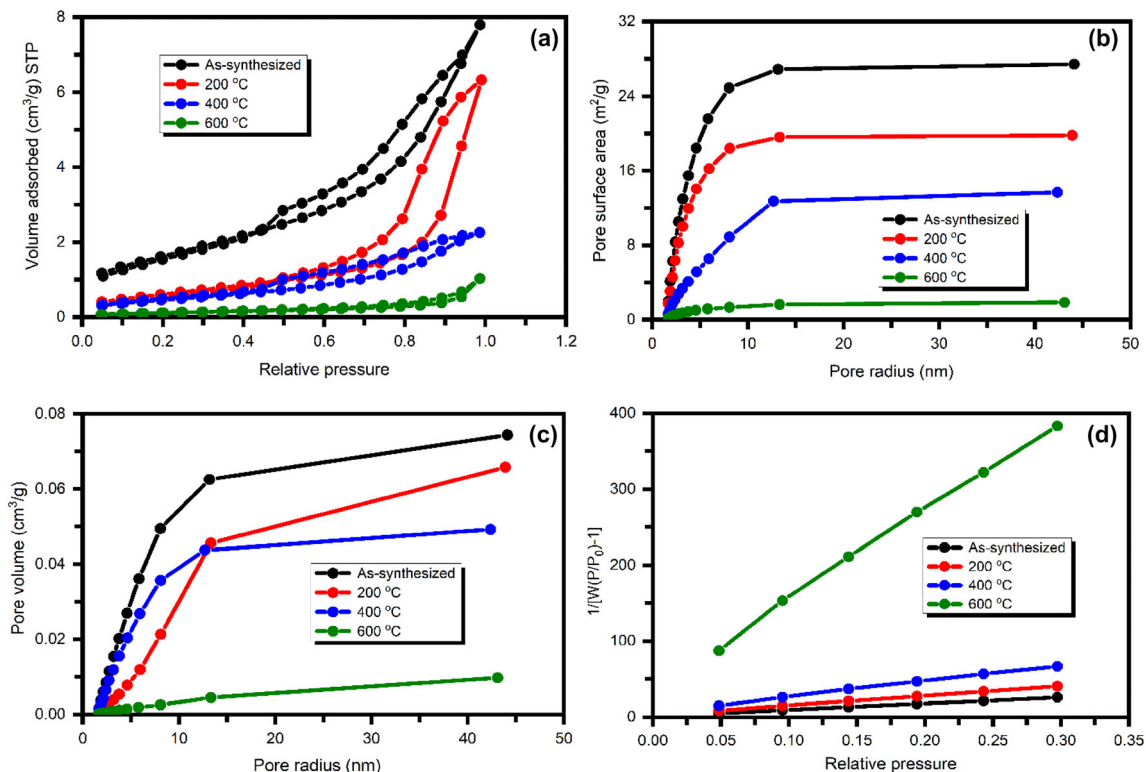

Fig. 9 **a** Nitrogen adsorption–desorption isotherms for TiO$_2$ at different annealing temperatures **b** and **c** BJH pore size distribution curve of TiO$_2$ **d** BET adsorption isotherm

Table 3 BET and BJH analysis parameters for rutile TiO$_2$ at the various annealing temperatures

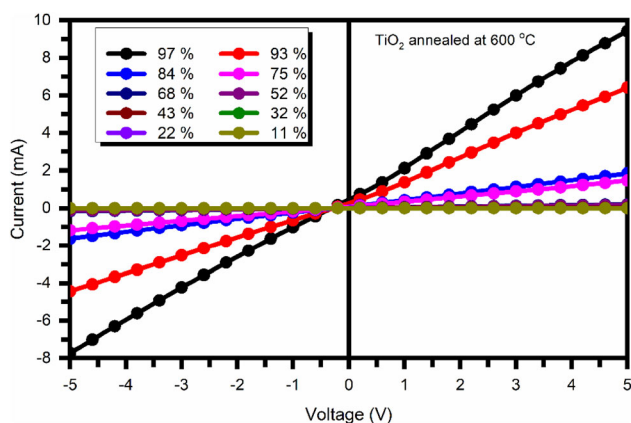| Sample	BET analysis			BJH pore size distribution	
	Surface area (m^2/g)	Average pore radius (nm)	Pore volume $\times 10^{-2}$ (cm^3/g)	Surface area (m^2/g)	Pore volume $\times 10^{-2}$ (cm^3/g)
TiO$_2$-RT	41.08	4.05	8.33	27.41	7.4
TiO$_2$-200	26.50	4.07	6.75	19.79	6.5
TiO$_2$-400	16.25	8.31	5.39	13.66	4.9
TiO$_2$-600	2.86	7.21	1.03	1.87	0.9

Fig. 10 I-V characteristics of hydrothermally grown rutile-TiO$_2$ microsphere (annealed at 600 °C) at different RH levels

600 °C) at different RH levels. As seen, the current increases with an increase in RH. These results confirm the semiconducting behavior of the as-synthesized and annealed rutile-TiO$_2$ microsphere. Due to double hydrogen bonding, the charge carrier cannot move freely in the chemisorbed layer at lower humidity. On the other hand, increasing humidity improves the bonding of water molecules with a hydroxyl group. As a result, it forms a physisorbed layer where carriers can quickly move [51] and increases the current. The humidity sensing properties of as-synthesized and annealed rutile-TiO$_2$ thin films were measured by monitoring the change in resistance with the corresponding change in relative humidity at room temperature (25 °C). The sensitivity was calculated using [52, 53],

$$S = \frac{R_{RH} - R_D}{R_D} \times 100\%, \qquad (6)$$

where R_{RH} is the saturated resistance of rutile-TiO$_2$ microsphere thin film at a given relative humidity and R_D is the stabilized resistance of dry air.

Figure 11 shows the variation of resistance of rutile-TiO$_2$ microsphere thin film as a function of change in relative humidity.

The error bars shown in the figure are derived from the differences obtained in resistance calculated for different relative humidity under the same set of prevailing experimental conditions. As seen, the resistance decreases with increase in relative humidity, which can be attributed to the mobility of charged carriers. When the rutile-TiO$_2$ nanoparticles film is exposed to low humidity, the water molecules are adsorbed on the TiO$_2$ surface and form a chemisorbed layer [54]. The tunneling effect of the electrons overcome the barrier between the chemisorbed layer and grain boundaries, which results in enhanced conduction in the rutile-TiO$_2$. Figure 12 shows the schematic illustration of the sensing mechanism in the rutile-TiO$_2$ films.

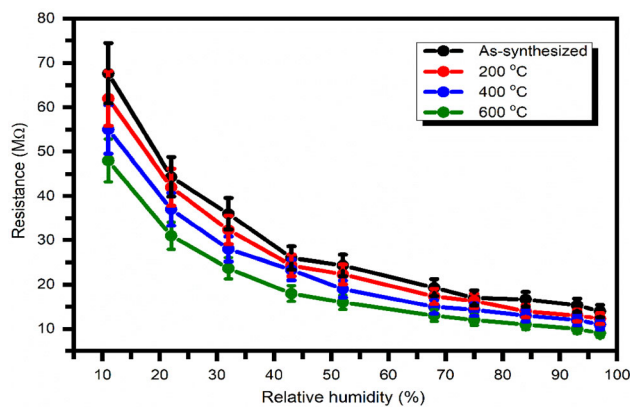Figure 13 shows the sensitivity of the humidity sensor fabricated using as-synthesized and annealed

Fig. 11 Variation of resistance of rutile-TiO$_2$ microsphere thin film as a function of change in relative humidity. The error bars shown in the figure are derived from the differences obtained in resistance calculated for all RH levels under the same set of prevailing experimental environments
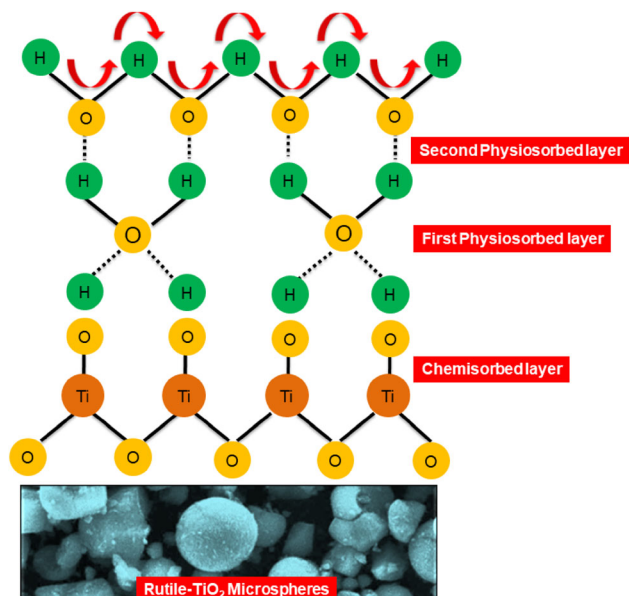
Fig. 12 Schematic illustration of TiO$_2$ humidity sensing mechanism (Grothuss conduction mechanism)

TiO$_2$ microsphere thin films at various relative humidity levels. The error bars shown in the figure are derived from the differences obtained in sensitivity calculated for different relative humidity under the same set of prevailing experimental conditions. The sensitivity monotonically increases with increase in relative humidity except for relative humidity of 11%. At low relative humidity (11%), few water molecules are adsorbed on TiO$_2$ microsphere film surfaces. As a result, a continuous water layer does not form. The proton hopping between the adjacent water molecules is difficult because of the immense activation energy [55, 56]. As the humidity level increases (22%), the water molecules adsorbed on the TiO$_2$ microsphere are enough to form a continuous water layer initially. As a result, proton conduction occurs, and the sensor shows relatively good sensitivity. When the relative humidity increased gradually to 97%, more water molecules were adsorbed on the TiO$_2$ microsphere film surface, and the water layer thickness increased. Increasing adsorbed water thickness on the sensing surface allows the water molecules to be ionized gradually under the electric field, and charge transport in the adsorbed water layer becomes convenient. Therefore, the sensitivity of the humidity sensor increases with increase in relative humidity.

Hysteresis is the non-coincidence between a particular plot's loading and unloading behavior. For
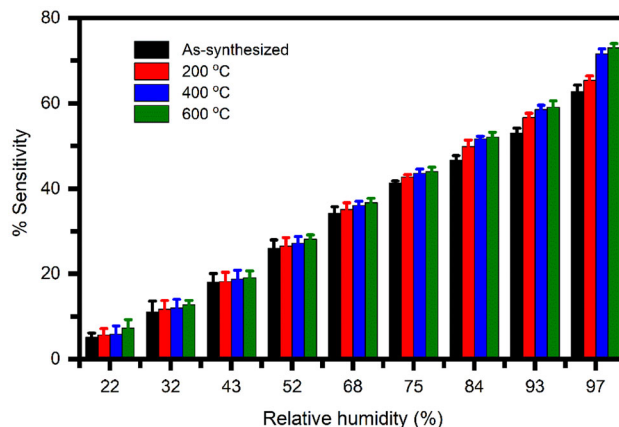

Fig. 13 Variation of the sensitivity of humidity sensor fabricated using as-synthesized and annealed TiO2 microsphere thin films at various relative humidity levels. The error bars shown in the figure are derived from the differences obtained in sensitivity calculated for all RH levels under the same set of prevailing experimental environments

example, a perfect humidity sensor's loading and unloading curves usually follow the same path. Figure 14 shows the hysteresis curves for humidity sensors fabricated using as-synthesized and annealed rutile-TiO$_2$ microspheres. When the relative humidity level increases from 11 to 97%, the water molecules are adsorbed on the TiO$_2$ surface, while they are desorbed when relative humidity decreases from 97 to 11%. As seen in Fig. 14a–d, the hysteresis loop becomes narrower with an increase in annealing temperature, signifying a decrease in the hysteresis loss. Humidity sensor fabricated using rutile-TiO$_2$ annealed at 600 °C show least hysteresis width hence better performance than the others.

Evaluating the performance of humidity sensors, response time, and recovery time are the most significant features. The response time of the humidity sensor is defined as the time required to reach 90% of the maximum resistance value observed under a higher humidity level. Similarly, the recovery time is defined as the time needed for the sensor when the resistance value drops to 10% of its maximum value [54, 57]. Thus, a good humidity sensor must have a rapid response and recovery time. The response and recovery were studied at a higher relative humidity (97%) and lower humidity level (22%) at room temperature at a bias voltage of 1 V. Figure 15 shows the variation of humidity sensors resistance as a function of time for humidity sensors fabricated using as-synthesized and annealed rutile-TiO$_2$ microspheres.
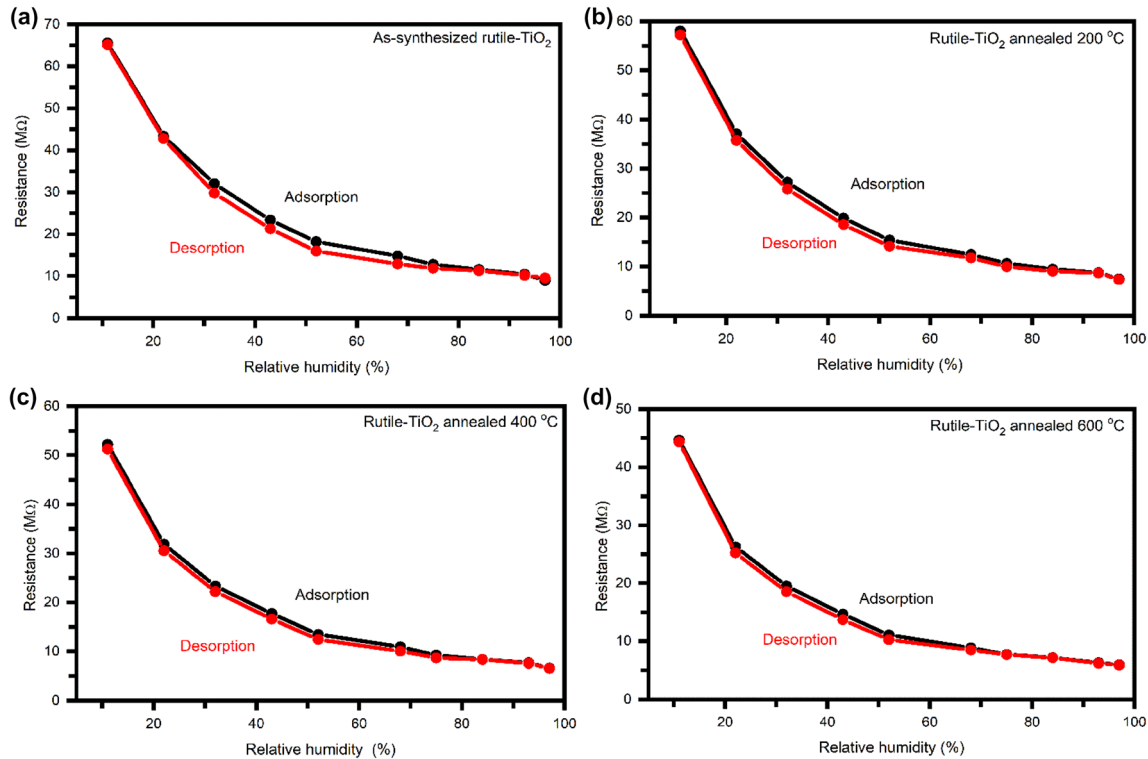
Fig. 14 Hysteresis curves for humidity sensors fabricated using as-synthesized and annealed rutile-TiO$_2$ microspheres

The humidity sensors response time is found to be 14.4 s, 12.1 s, 15.8 s, and 11.1 s for as-synthesized and annealed TiO$_2$ at 200 °C, 400 °C, and 600 °C respectively, while the recovery time is found to be 1.5 s, 2.9 s, 1.9 s, and 0.8 s for as-synthesized and annealed TiO$_2$ at 200 °C, 400 °C, and 600 °C respectively. The rapid response and recovery time (11.1 s and 0.8 s) observed the humidity sensor fabricated using rutile-TiO$_2$ microspheres annealed at 600 °C. The fast recovery time may be due to the fast desorption process of H$_2$O molecules from the TiO$_2$ surface. Besides, it is observed that the rutile-TiO$_2$ microspheres humidity sensor produces a repeatable change in resistance on exposure to RH and shows a constant value of baseline resistance, indicating stable device behavior. Table 4 shows the response and recovery time of the hierarchical nanostructure of TiO$_2$ based humidity sensors reported earlier.

As seen, the hydrothermally grown TiO$_2$ microsphere humidity sensor shows a fast response and recovery time compared with other oxide-based humidity sensors at higher humidity.

Stability and repeatability are important parameters for the humidity sensors. The present work tested the TiO$_2$ microsphere humidity sensor for stability and repeatability under fixed relative humidity levels (22% and 97%). The results are shown in Fig. 16. It is observed that the current in the TiO$_2$ microsphere humidity sensor increases with increase in annealing temperature. Thus, enhancement in current and humidity sensing performance is due to an improvement in the crystallinity in TiO$_2$ with increase in annealing temperature. Furthermore, it is observed that the TiO$_2$ microsphere humidity sensor produces a repeatable change in current on exposure to relative humidity and shows a constant value of baseline current, indicating stable device behavior.

4 Conclusions

This paper reports the synthesis of rutile-TiO$_2$ microsphere thin films using the hydrothermal method. The effect of annealing temperature on structural, optical, morphological, and humidity sensing properties have been investigated. No diffraction peaks due to anatase or brookite phase have been detected in the X-ray diffraction pattern,
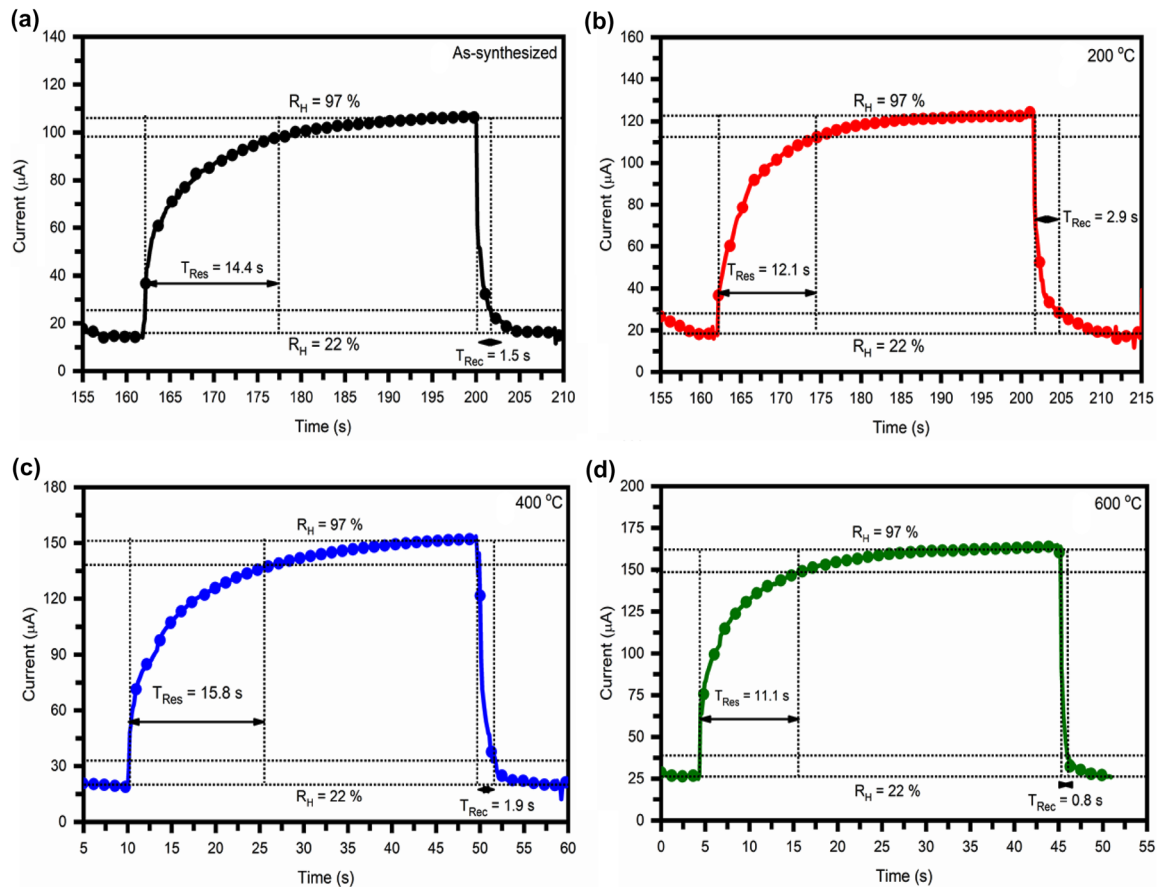
Fig. 15 Variation of sensors resistance as a function of time for humidity sensors fabricated using as-synthesized and annealed rutile-TiO$_2$ microspheres

Table 4 Comparison of response and recovery time of the hierarchical nanostructure of TiO$_2$-based humidity sensors

Sensing material	Synthesis method	Response time (s)	Recovery time (s)	Refs.
TiO$_2$ nanoflowers	Hydrothermal	143	33	[58]
TiO$_2$ nanotubes	Anodic oxidation	100	190	[34]
TiO$_2$ nanowires	Hydrothermal	< 90	< 90	[35]
TiO$_2$ nanosheets	Self-assembly	3	50	[59]
TiO$_2$ nanofibre	Electrospinning	1	4	[60]
TiO$_2$ nanoweb	Spray pyrolysis	57.5	3	[61]
TiO$_2$ nanorods	Wet chemical method	20	33	[62]
TiO$_2$ microspheres	Hydrothermal	11	0.8	Present work

ensuring the formation of high-purity rutile-TiO$_2$ using the hydrothermal method. The most intense peak corresponds to the (110) plane, and its intensity increases with an increase in annealing temperature, signifying an enhancement in the film's crystallinity. Furthermore, the highly intense and sharp Raman peaks indicate the highly crystalline nature of as-synthesized and annealed TiO$_2$ materials. Surface morphology investigated by scanning electron microscopy analysis shows the formation of uniform

and homogeneous microspheres-like morphology throughout the substrate surface without flaws and cracks. UV–Visible spectroscopy analysis showed no significant change in the band gap with an increase in annealing temperature. Finally, humidity sensors using as-synthesized and annealed TiO$_2$ were fabricated on the interdigital electrode pattern to evaluate their sensing performance. The sensors showed good sensing properties in a wide relative humidity range from 11 to 97%. The humidity sensor fabricated with
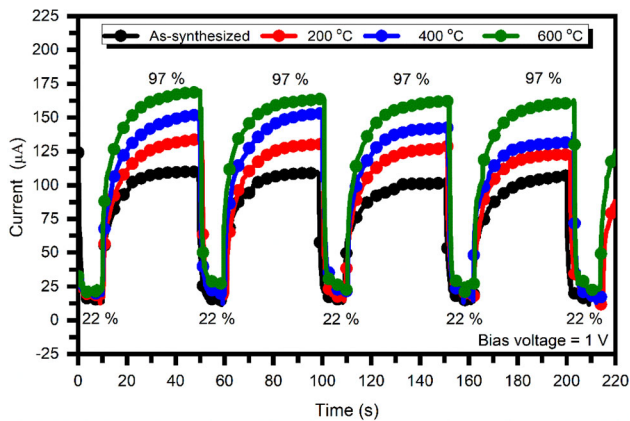
Fig. 16 Stability and repeatability tests under fixed relative humidity levels (22% and 97%) of TiO_2 microsphere humidity sensors

rutile-TiO_2 microspheres annealed at 600 °C showed the highest sensitivity ($\sim$ 72%), having a fast response time ($\sim$ 11.1 s) and recovery time ($\sim$ 0.8 s). The results demonstrate that the rutile-TiO_2 microsphere-based humidity sensors fabricated on an interdigital electrode pattern can be better for humidity sensors than fabricated on the traditional FTO substrate.

Acknowledgements

Author contributions

YH: Writing-original draft, Data curation, Formal analysis. VS: Investigation, Methodology. VD: Data curation, Methodology. AW: Data curation, Methodology. AP: Data curation, Methodology. PS: Data curation, Methodology. SS: Data curation, Methodology. SR: Data curation, Methodology. PV: Data curation, Methodology. BB: Formal analysis. YJ: Writing-review and editing. MP: Investigation, Methodology. SR: Validation, Methodology. AR: Validation, Methodology. SJ: Writing-review and editing, Supervision, Funding acquisition On the behalf of all authors.

Funding

Data availability

We hereby declare that the data/results are original and have not been communicated for publication elsewhere, have not been published previously, and are not under consideration for publication elsewhere. Therefore, if accepted, the data/results will not be published elsewhere.

Declarations

Conflict of interest The authors declare that they have no known competing financial interests or personal relationships that could have influenced the work reported in this paper.

Ethical statement This article does not contain any studies with human participants or animals performed by any authors.

References

1. K. Sager, A. Schroth, A. Nakladal, G. Gerlach, Humidity-dependent mechanical properties of polyimide films and their use for IC-compatible humidity sensors. Sens. Actuators A **53**, 330–334 (1996). https://doi.org/10.1016/0924-4247(96)01132-6

2. N. Ikeda, R. Shigeta, J. Shiomi, Y. Kawahara, Soil-Monitoring Sensor Powered by Temperature Difference between Air

and Shallow Underground Soil. Proc. ACM Interactive Mobile Wearable Ubiquitous Technol. **4**, 1–22 (2020). https://doi.org/10.1145/3380995

3. C.D. Feng, S.L. Sun, H. Wang, C.U. Segre, J.R. Stetter, Humidity sensing properties of Nation and sol-gel derived SiO_2/Nafion composite thin films. Sens. Actuators B **40**, 217–222 (1997). https://doi.org/10.1016/S0925-4005(97)80265-1

4. S. Ghosh, R. Ghosh, P.K. Guha, T.K. Bhattacharyya, Humidity sensor based on high proton conductivity of graphene oxide. IEEE Trans. Nanotechnol. **14**, 931–937 (2015). https://doi.org/10.1109/TNANO.2015.2465859

5. H. Guo, J. Chen, L. Tian, Q. Leng, Y. Xi, C. Hu, Airflow-Induced triboelectric nanogenerator as a self-powered sensor for detecting humidity and airflow rate. ACS Appl. Mater. Interfaces. **6**, 17184–17189 (2014). https://doi.org/10.1021/am504919w

6. Z. Chen, C. Lu, Humidity sensors: a review of materials and mechanisms. Sens. Lett. **3**, 274–295 (2005). https://doi.org/10.1166/sl.2005.045

7. A. Sun, L. Huang, Y. Li, Study on humidity sensing property based on TiO_2 porous film and polystyrene sulfonic sodium. Sens. Actuators B **139**, 543–547 (2009). https://doi.org/10.1016/j.snb.2009.03.064

8. W.P. Tai, J.H. Oh, Fabrication and humidity sensing properties of nanostructured TiO_2–SnO_2 thin films. Sens. Actuators B **85**, 154–157 (2002). https://doi.org/10.1016/S0925-4005(02)00074-6

9. A.I. Buvailo, Y. Xing, J. Hines, N. Dollahon, E. Borguet, TiO_2/LiCl-based nanostructured thin film for humidity sensor applications. ACS Appl. Mater. Interfaces **3**, 528–533 (2011). https://doi.org/10.1021/am1011035

10. P.M. Faia, C.S. Furtado, A.J. Ferreira, Humidity sensing properties of a thick-film titania prepared by a slow spinning proces. Sens. Actuators B **101**, 183–190 (2004). https://doi.org/10.1016/j.snb.2004.02.050

11. S. Agarwal, G.L. Sharma, Humidity sensing properties of (Ba, Sr) TiO_3 thin films grown by hydrothermal–electrochemical method. Sens. Actuators B **85**, 205–211 (2002). https://doi.org/10.1016/S0925-4005(02)00109-0

12. J.J. Steele, M.T. Taschuk, M.J. Brett, Nanostructured metal oxide thin films for humidity sensors. IEEE Sens. J. **8**, 1422–1429 (2008). https://doi.org/10.1109/JSEN.2008.920715

13. G. Wang, Q. Wang, W. Lu, J. Li, Photoelectrochemical study on charge transfer properties of TiO_2 −B nanowires with an application as humidity sensors. J. Phys. Chem. B **110**, 22029–22034 (2006). https://doi.org/10.1021/jp064630k

14. W.M. Campbell, A.K. Burrell, D.L. Officer, K.W. Jolley, Porphyrins as light harvesters in the dye-sensitised TiO_2 solar cell. Coord. Chem. Rev. **248**, 1363–1379 (2004). https://doi.org/10.1016/j.ccr.2004.01.007

15. V. Bairi, S. Bourdo, N. Sacre, D. Nair, B. Berry, A. Biris, T. Viswanathan, Ammonia gas sensing behavior of tanninsulfonic acid doped polyaniline-TiO_2 composite. Sensors. **15**, 26415–26429 (2015). https://doi.org/10.3390/s151026415

16. E. Garofalo, L. Cecchini, M. Bevione, A. Chiolerio, Triboelectric characterization of colloidal TiO_2 for energy harvesting applications. Nanomaterials **10**, 1181 (2020). https://doi.org/10.3390/nano10061181

17. Y.C. Lee, Y.P. Hong, H.Y. Lee, H. Kim, Y.J. Jung, K.H. Ko, H.S. Jung, K.S. Hong, Photocatalysis and hydrophilicity of doped TiO_2 thin films. J. Colloid Interface Sci. **267**, 127–131 (2003). https://doi.org/10.1016/S0021-9797(03)00603-9

18. L. Wang, R. Wang, L. Feng, Y. Liu, Coupling TiO_2 nanorods with g-CN using modified physical vapor deposition for efficient photoelectrochemical water oxidation. J. Am. Ceram. Soc. **103**, 6272–6279 (2020). https://doi.org/10.1111/jace.17335

19. P.S. Jadhav, T. Jadhav, M. Bhosale, C.H. Jadhav, V.C. Pawar, Structural and optical properties of N-doped TiO_2 nanomaterials. Mater. Today Proc. **43**, 2763–2767 (2021). https://doi.org/10.1016/j.matpr.2020.07.164

20. C.H. Wu, K.S. Huang, J.-M. Chern, Decomposition of acid dye by TiO_2 thin films prepared by the sol−gel method. Ind. Eng. Chem. Res. **45**, 2040–2045 (2006). https://doi.org/10.1021/ie051068w

21. J. Li, N. Lu, X. Quan, S. Chen, H. Zhao, Facile method for fabricating boron-doped TiO_2 nanotube array with enhanced photoelectrocatalytic properties. Ind. Eng. Chem. Res. **47**, 3804–3808 (2008). https://doi.org/10.1021/ie0712028

22. A. Borras, J.R. Sanchez-Valencia, R. Widmer, V.J. Rico, A. Justo, A.R. Gonzalez-Elipe, Growth of crystalline TiO_2 by plasma enhanced chemical vapor deposition. Cryst. Growth Des. **9**, 2868–2876 (2009). https://doi.org/10.1021/cg9001779

23. K. Nagaveni, M.S. Hegde, G. Madras, Structure and photocatalytic activity of Ti 1–x M x O 2±δ (M = W, V, Ce, Zr, Fe, and Cu) synthesized by solution combustion method. J. Phys. Chem. B **108**, 20204–20212 (2004). https://doi.org/10.1021/jp047917v

24. A. Mamakhel, C. Tyrsted, E.D. Bøjesen, P. Hald, B.B. Iversen, Direct formation of crystalline phase pure rutile TiO_2 nanostructures by a facile hydrothermal method. Cryst. Growth Des. **13**, 4730–4734 (2013). https://doi.org/10.1021/cg400858p

25. Y. Zhang, K. Yu, D. Jiang, Z. Zhu, H. Geng, L. Luo, Zinc oxide nanorod and nanowire for humidity sensor. Appl. Surf. Sci. **242**, 212–217 (2005). https://doi.org/10.1016/j.apsusc.2004.08.013

26. X. Wang, Y. Sang, D. Wang, S. Ji, H. Liu, Enhanced gas sensing property of SnO_2 nanoparticles by constructing the SnO_2–TiO_2 nanobelt heterostructure. J. Alloys Compd. **639**, 571–576 (2015). https://doi.org/10.1016/j.jallcom.2015.03.193

27. T. Santhaveesuk, D. Wongratanaphisan, S. Choopun, Enhancement of sensor response by TiO_2 mixing and Au coating on ZnO tetrapod sensor. Sens. Actuators B **147**, 502–507 (2010). https://doi.org/10.1016/j.snb.2010.03.081

28. Y. Lai, Y. Tang, J. Gong, D. Gong, L. Chi, C. Lin, Z. Chen, Transparent superhydrophobic/superhydrophilic TiO_2-based coatings for self-cleaning and anti-fogging. J. Mater. Chem. **22**, 7420 (2012). https://doi.org/10.1039/c2jm16298a

29. D. Sarkar, K.K. Chattopadhyay, Branch density-controlled synthesis of hierarchical TiO_2 nanobelt and tunable three-step electron transfer for enhanced photocatalytic property. ACS Appl. Mater. Interfaces. **6**, 10044–10059 (2014). https://doi.org/10.1021/am502379q

30. Y.J. Hwang, C. Hahn, B. Liu, P. Yang, Photoelectrochemical properties of TiO_2 nanowire arrays: a study of the dependence on length and atomic layer deposition coating. ACS Nano **6**, 5060–5069 (2012). https://doi.org/10.1021/nn300679d

31. J. Harris, R. Silk, M. Smith, Y. Dong, W.T. Chen, G.I.N. Waterhouse, Hierarchical TiO_2 nanoflower photocatalysts with remarkable activity for aqueous methylene blue photo-oxidation. ACS Omega **5**, 18919–18934 (2020). https://doi.org/10.1021/acsomega.0c02142

32. S.P. Hong, J. Park, S.S.M. Bhat, T.H. Lee, S.A. Lee, K. Hong, M.-J. Choi, M. Shokouhimehr, H.W. Jang, Comprehensive study on the morphology control of TiO_2 nanorods on foreign substrates by the hydrothermal method. Cryst. Growth Des. **18**, 6504–6512 (2018). https://doi.org/10.1021/acs.cgd.8b00609

33. L.L.W. Chow, M.M.F. Yuen, P.C.H. Chan, A.T. Cheung, Reactive sputtered TiO_2 thin film humidity sensor with negative substrate bias. Sens. Actuators B **76**, 310–315 (2001). https://doi.org/10.1016/S0925-4005(01)00602-5

34. Y. Zhang, W. Fu, H. Yang, Q. Qi, Y. Zeng, T. Zhang, R. Ge, G. Zou, Synthesis and characterization of TiO_2 nanotubes for humidity sensing. Appl. Surf. Sci. **254**, 5545–5547 (2008). https://doi.org/10.1016/j.apsusc.2008.02.106

35. R.J. Wu, Y.L. Sun, C.C. Lin, H.-W. Chen, M. Chavali, Composite of TiO_2 nanowires and Nafion as humidity sensor material. Sens. Actuators B **115**, 198–204 (2006). https://doi.org/10.1016/j.snb.2005.09.001

36. P.G. Su, L.N. Huang, Humidity sensors based on TiO_2 nanoparticles/polypyrrole composite thin films. Sens. Actuators B **123**, 501–507 (2007). https://doi.org/10.1016/j.snb.2006.09.052

37. A. Kassas, J. Bernard, C. Lelièvre, A. Besq, Y. Guhel, D. Houivet, B. Boudart, H. Lakiss, T. Hamieh, Ceramic thick film humidity sensor based on MgTiO3+LiF. Mater. Res. Bull. **48**, 3987–3993 (2013). https://doi.org/10.1016/j.materresbull.2013.06.010

38. Y. Zhao, B. Yang, J. Liu, Effect of interdigital electrode gap on the performance of SnO_2-modified MoS2 capacitive humidity sensor. Sens. Actuators B **271**, 256–263 (2018). https://doi.org/10.1016/j.snb.2018.05.084

39. S. Yu, H. Zhang, J. Zhang, Synthesis of high response gold/titanium dioxide humidity sensor and its application in human respiration. Ceram. Int. **47**, 30880–30887 (2021). https://doi.org/10.1016/j.ceramint.2021.07.270

40. H. Huang, X. Hou, J. Xiao, L. Zhao, Q. Huang, H. Chen, Y. Li, Effect of annealing atmosphere on the performance of TiO_2 nanorod arrays in photoelectrochemical water splitting. Catal. Today. **330**, 189–194 (2019). https://doi.org/10.1016/j.cattod.2018.04.011

41. B.D.C. and S.R. Stock, No Title Elements of X-ray Diffraction. Third Edition, (2001)

42. H. Zhao, J. Xie, T. Liang, A. Mao, A. Wang, Y. Chen, D. Ma, V. Paley, A.A. Volinsky, Effects of thickness ratios and sputtering mode on the structural, electrical and optical properties of bilayer molybdenum thin films. AIP Adv. **8**, 095028 (2018). https://doi.org/10.1063/1.5043437

43. B. Bade, S. Rondiya, S. Bhopale, N. Dzade, M. Kamble, A. Rokade, M. Nasane, M. More, A. Funde, Investigation of growth mechanism for highly oriented TiO_2 nanorods: the role of reaction time and annealing temperature. SN Appl. Sci. **1**, 1073 (2019). https://doi.org/10.1007/s42452-019-0978-2

44. C.D. Mazza, T.E. Barborini, P. Piseri, P. Milani, D. Cattaneo, A.L. Bassi, CARLO ENRICO Bottani, Raman spectroscopy characterization of TiO_2 rutile nanocrystals. Phys. Rev. B **4**, 045416 (2007). https://doi.org/10.1103/PhysRevB.75.045416

45. G. Kortum, *Reflectance Spectroscopy: Principles, Methods* (Applications. Springer, New York, 1969)

46. M. Naderi, Surface Area, in: Prog. Filtr. Sep., Elsevier,: pp. 585–608 (2015). https://doi.org/10.1016/B978-0-12-384746-1.00014-8.

47. R. Bardestani, G.S. Patience, S. Kaliaguine, Experimental methods in chemical engineering: specific surface area and pore size distribution measurements—BET, BJH, and DFT. Can. J. Chem. Eng. **97**, 2781–2791 (2019). https://doi.org/10.1002/cjce.23632

48. K. Sing, The use of nitrogen adsorption for the characterisation of porous materials. Colloids Surf. A **187–188**, 3–9 (2001). https://doi.org/10.1016/S0927-7757(01)00612-4

49. M. Hakamada, T. Kuromura, Y. Chen, H. Kusuda, M. Mabuchi, Influence of porosity and pore size on electrical

resistivity of porous aluminum produced by spacer method. Mater. Trans. **48**, 32–36 (2007). https://doi.org/10.2320/matertrans.48.32

50. P.S. Liu, T.F. Li, C. Fu, Relationship between electrical resistivity and porosity for porous metals. Mater. Sci. Eng. A **268**, 208–215 (1999). https://doi.org/10.1016/S0921-5093(99)00073-8

51. A.S. Pawbake, R.G. Waykar, D.J. Late, S.R. Jadkar, Highly transparent wafer-scale synthesis of crystalline WS_2 nanoparticle thin film for photodetector and humidity-sensing applications. ACS Appl. Mater. Interfaces. **8**, 3359–3365 (2016). https://doi.org/10.1021/acsami.5b11325

52. R. Aher, A. Bhorde, S. Nair, H. Borate, S. Pandharkar, D. Naik, P. Vairale, S. Karpe, D. Late, M. Prasad, S. Jadkar, Solvothermal growth of $PbBi_2Se_4$ nano-flowers: a material for humidity sensor and photodetector applications. Phys. Status Solidi. **216**, 1900065 (2019). https://doi.org/10.1002/pssa.201900065

53. S.A. Arote, A.S. Pathan, Y.V. Hase, P.P. Bardapurkar, D.L. Gapale, B.M. Palve, Investigations on synthesis, characterization and humidity sensing properties of ZnO and $ZnO-ZrO_2$ composite nanoparticles prepared by ultrasonic assisted wet chemical method. Ultrason. Sonochem. **55**, 313–321 (2019). https://doi.org/10.1016/j.ultsonch.2019.01.012

54. P.R. Mudimela, K. Grigoras, I.V. Anoshkin, A. Varpula, V. Ermolov, A.S. Anisimov, A.G. Nasibulin, S. Novikov, E.I. Kauppinen, Single-walled carbon nanotube network field effect transistor as a humidity sensor. J. Sensors. **2012**, 1–7 (2012). https://doi.org/10.1155/2012/496546

55. G. Zhao, J. Xuan, Q. Gong, L. Wang, J. Ren, M. Sun, F. Jia, G. Yin, B. Liu, In situ growing double-layer TiO_2 nanorod arrays on new-type FTO electrodes for low-concentration NH_3 detection at room temperature. ACS Appl. Mater. Interfaces. **12**, 8573–8582 (2020). https://doi.org/10.1021/acsami.9b20337

56. Z. Wang, L. Shi, F. Wu, S. Yuan, Y. Zhao, M. Zhang, The sol–gel template synthesis of porous TiO_2 for a high performance humidity sensor. Nanotechnology **22**, 275502 (2011). https://doi.org/10.1088/0957-4484/22/27/275502

57. Q. Kuang, C. Lao, Z.L. Wang, Z. Xie, L. Zheng, High-sensitivity humidity sensor based on a single SnO_2 nanowire. J. Am. Chem. Soc. **129**, 6070–6071 (2007). https://doi.org/10.1021/ja070788m

58. P.V. Shinde, S. Gagare, C.S. Rout, D.J. Late, TiO_2 nanoflowers based humidity sensor and cytotoxic activity. RSC Adv. **10**, 29378–29384 (2020). https://doi.org/10.1039/D0RA05007E

59. M. Gong, Y. Li, Y. Guo, X. Lv, X. Dou, 2D TiO_2 nanosheets for ultrasensitive humidity sensing application benefited by abundant surface oxygen vacancy defects. Sens. Actuators B **262**, 350–358 (2018). https://doi.org/10.1016/j.snb.2018.01.187

60. H. Jamil, S.S. Batool, Z. Imran, M. Usman, M.A. Rafiq, M. Willander, M.M. Hassan, Electrospun titanium dioxide nanofiber humidity sensors with high sensitivity. Ceram. Int. **38**, 2437–2441 (2012). https://doi.org/10.1016/j.ceramint.2011.11.010

61. D.L. Gapale, S.A. Arote, B.M. Palve, S.N. Dalvi, R.Y. Borse, Effect of film thickness on humidity sensing of spray deposited TiO_2 thin films. Mater. Res. Express. **6**, 026402 (2018). https://doi.org/10.1088/2053-1591/aae970

62. N. Chaurasiya, U. Kumar, S. Sikarwar, B.C. Yadav, P.K. Yadawa, Synthesis of TiO_2 nanorods using wet chemical method and their photovoltaic and humidity sensing applications. Sensors Int. **2**, 100095 (2021). https://doi.org/10.1016/j.sintl.2021.100095

Publisher's Note Springer Nature remains neutral with regard to jurisdictional claims in published maps and institutional affiliations.